THE JOURNAL OF PHYSICAL CHEMISTRY B

Article

pubs.acs.org/JPCB

Radical Reactions Affecting Polar Groups in Threonine Peptide Ions

Huong T. H. Nguyen,[†,§] Prokopis C. Andrikopoulos,[‡,§] Daniel Bím,[‡] Lubomír Rulíšek,[‡] Andy Dang,[†] and František Tureček*[,†]

[†]Department of Chemistry, University of Washington, Bagley Hall, Box 351700, Seattle, Washington 98195-1700, United States

[‡]Institute of Organic Chemistry and Biochemistry, Czech Academy of Sciences, Flemingovo nám 2, 16610 Prague, Czech Republic

Supporting Information

ABSTRACT: Peptide cation-radicals containing the threonine residue undergo radical-induced dissociations upon collisional activation and photon absorption in the 210−400 nm range. Peptide cation-radicals containing a radical defect at the *N*-terminal residue, [•Ala-Thr-Ala-Arg+H]$^+$, were generated by electron transfer dissociation (ETD) of peptide dications and characterized by UV−vis photodissociation action spectroscopy combined with time-dependent density functional theory (TD-DFT) calculations of absorption spectra, including thermal vibronic band broadening. The action spectrum of [•Ala-Thr-Ala-Arg+H]$^+$ ions was indicative of the canonical structure of an *N*-terminally deaminated radical whereas isomeric structures differing in the position of the radical defect and amide bond geometry were excluded. This indicated that exothermic electron transfer to threonine peptide ions did not induce radical isomerizations in the fragment cation-radicals. Several isomeric structures, ion−molecule complexes, and transition states for isomerizations and dissociations were generated and analyzed by DFT and Møller−Plesset perturbational ab initio calculations to aid interpretation of the major dissociations by loss of water, hydroxyl radical, $C_3H_6NO^•$, C_3H_7NO, and backbone cleavages. Born−Oppenheimer molecular dynamics (BOMD) in combination with DFT gradient geometry optimizations and intrinsic reaction coordinate analysis were used to search for low-energy cation-radical conformers and transition states. BOMD was also employed to analyze the reaction trajectory for loss of water from ion−molecule complexes.

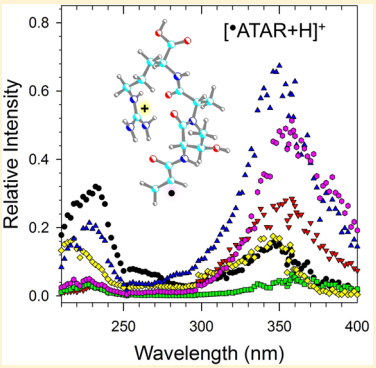

INTRODUCTION

Whereas most peptide and protein chemical reactions involve polar groups with closed electronic shells, there is a growing cohort of biological reactions that are known to proceed via radical intermediates. For example, radical intermediates play a role in several redox enzyme reactions,[1−8] and most recently, a glycyl radical enzyme has been found to metabolize hydroxyproline in human gut microbiome.[9] Peptide and protein radicals can be formed by hydrogen abstraction or oxidative processes involving reactive radical species or transition metals that affect, respectively, the C_α-H bonds of the backbone or oxidation-prone side chains, such as those in cysteine, tyrosine and tryptophan.[10] Peptide-related radicals have received considerable attention regarding their thermodynamic stability and its relationship to the backbone conformation.[11−15] Recently, methods have been developed to generate peptide radicals as isolated species in the gas phase using electron transfer reactions and mass spectrometric product analysis. One of these methods, introduced by Siu and co-workers,[16] uses oxidative intramolecular electron transfer in ternary transition metal-peptide ion complexes[17,18] in the gas phase to produce peptide cation-radicals that are stochiometrically equivalent to neutral peptide molecules and do not contain additional charging protons.[19] These so-called hydrogen-deficient peptide cation radicals are isolated by mass and studied by methods of gas-phase ion chemistry. For example, structures of hydrogen-deficient peptide cation radicals have been studied by multiphoton infrared photodissociation action spectroscopy (IRMPD)[20] and UV−vis photodissociation action spectroscopy.[21,22] A different type of peptide cation radicals are produced by one-electron reduction of multiply protonated peptide ions.[19] Such peptide radicals are called hydrogen-rich[23] and often occur as short-lived reaction intermediates that dissociate by backbone and side-chain cleavages. Peptide cation-radical dissociations have been extensively utilized for protein sequence analysis by electron capture[24] and electron transfer dissociation[25] methods of tandem mass spectrometry, and determining the structure and electronic properties of peptide cation-radicals and their dissociation products have been of considerable interest.[19]

Cleavage of backbone bonds between the amide nitrogen and the adjacent α carbon of the same residue (N−C_α bond cleavage) is a common radical-triggered dissociation in hydrogen-rich protein and peptide cation radicals.[19] These cleavages produce cation-radicals corresponding to deaminated and truncated C-terminal peptide fragments which are called $[z_n+H]^{+•}$ ions (Scheme 1).[26] These ions typify unusual structures called distonic ions,[27,28] in which the radical and

Received: May 15, 2017
Revised: June 13, 2017
Published: June 14, 2017

DOI: 10.1021/acs.jpcb.7b04661
J. Phys. Chem. B 2017, 121, 6557−6569

Scheme 1. Formation of $[z_4+H]^{+\bullet}$ Ions from $[AATAR+2H]^{2+}$

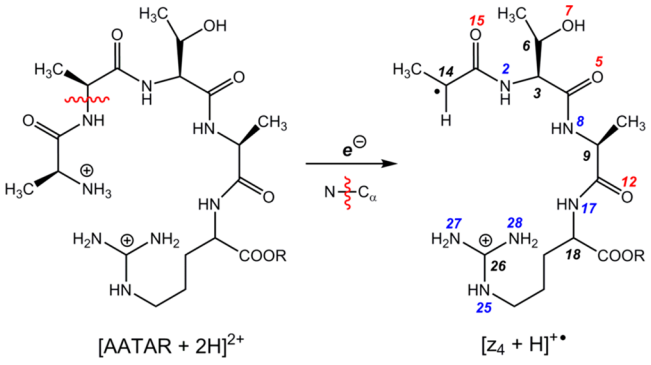

ion sites reside on different and distant atoms. In addition to being of theoretical interest because of their unusual structures, ions of the $[z_n+H]^{+\bullet}$ type have also attracted considerable attention because they retain information on the peptide fragment's amino acid sequence that can be further mined by tandem mass spectrometry via consecutive radical backbone dissociations.[29−33] A particularly important question in this respect is whether the $[z_n+H]^{+\bullet}$ ions retain their canonical structure related to the original peptide ion or undergo radical-driven molecular rearrangements.

To address these questions, structures of hydrogen-rich peptide cation radicals in the gas phase have been recently studied by UV−vis action spectroscopy,[34] and several $[z_n+H]^{+\bullet}$ ions have been studied by UVPD[21] and IRMPD.[20] Action spectroscopy is a photodissociative method in which resonant absorption of one or multiple photons by a gas-phase ion triggers dissociation ("action") that is detected by mass spectrometry.[35,36] These studies, that so far have been limited to Asp, Phe, Trp, and His, have revealed that the propensity for spontaneous isomerization of $[z_n+H]^{+\bullet}$ ions depended on the amino acid residues in the ion.[20,21] In addition to recent spectroscopic studies, $[z_n+H]^{+\bullet}$ ions have been the subject of investigations that focused on elucidating the collision-induced dissociation mechanisms, kinetics, and characterizing dissociation products. Both survey[37,38] and mechanistic studies[39,40] have been reported that addressed the competition between backbone and side-chain dissociations in peptide cation-radicals, depending on the nature and sequence of amino acid residues. In particular, the complex chemistry of serine-containing peptide cation radicals has been addressed by studies that pointed out competitive dissociations involving the backbone and side chain groups.[41,42]

Previous mechanistic studies of peptide cation-radical chemistry have been aided by ab initio and density functional theory calculations of ion structures, transition states, and UV−vis absorption spectra. Theoretical calculations of gas-phase peptide ion structures are notoriously difficult because of the multitude of tautomers and conformers that have to be considered to adequately describe the potential energy surface.[43] This is further emphasized in computational studies of transition states for peptide ion dissociations where small changes of energy can have large effects on the calculated unimolecular rate constants and branching ratios.[42] It is therefore important to anchor the calculations to experimental data obtained by spectroscopy or ion mobility measurements.[43] Here, we combine experimental action spectroscopy and computational methods to elucidate the structure, reaction mechanisms, and dynamics of dissociations of $[z_4+H]^{+\bullet}$ ions containing the polar threonine residue. As models we chose *N*-terminally deaminated tryptic cation radicals ($^{\bullet}$Ala-Thr-Ala-Arg +H)$^+$ and ($^{\bullet}$Ala-Thr-Ala-Arg-OCH_3+H)$^+$ in which the charging proton is sequestered at the arginine residue, thus removing the ambiguity of locating the charge site. The C-terminal methyl ester was used to distinguish the threonine side-chain and terminal carboxyl hydroxyl groups.

The article is organized as follows. First we present and analyze unimolecular dissociations of $[z_4+H]^{+\bullet}$ ions containing Thr. Next, we present spectroscopic evidence of the $[z_4+H]^{+\bullet}$ ion structure. Finally, we use density functional theory (DFT) and Born−Oppenheimer molecular dynamics (BOMD) calculations to analyze the energetics and dynamics of isomerizations and dissociations triggered by collisional activation. We wish to show that the threonine residue does not promote spontaneous isomerizations in the $[z_4+H]^{+\bullet}$ ions formed by electron transfer dissociation. Upon collisional activation and photodissociation, the side chain substantially participates in radical reactions that characterize the threonine residue for peptide sequencing by mass spectrometry.

EXPERIMENTAL SECTION

Materials. The Ala-Ala-Thr-Ala-Arg (AATAR) peptide was custom-synthesized at >90% purity by GenScript (Piscataway, NJ, USA), and the received sample was checked by electrospray ionization mass spectrometry. The amino acid sequence was checked by an electron-transfer dissociation (ETD) mass spectrum that showed the expected sequence fragment ions of the $[z_n+H]^{+\bullet}$ type (Figure S1a, Supporting Information). The AATAR methyl ester was prepared by esterification of AATAR in anhydrous methanol, as described previously,[44] and characterized by its ETD mass spectrum (Figure S1b).

Methods. ETD mass spectra and photodissociation action (UVPD) spectra were measured on a ThermoElectron Fisher (San Jose, CA, USA) LTQ-XL-ETD linear ion trap mass spectrometer equipped with an external EKSPLA NL301G (Altos Photonics, Bozeman, MT) Nd:YAG laser source operating at a frequency of 20 Hz with a 3−6 ns pulse width, as described previously.[21] The pump laser was interfaced to the LTQ via LabView software (National Instruments, Austin, TX). Briefly, photons from the pump were directed into a PG142C unit (Altos Photonics) consisting of a third harmonic generator and optical parametric oscillator coupled with an optional second harmonic generator, that provided wavelength tuning between 210−700 nm at 0.52−12.69 mJ per pulse. The power of the PG142C output beam was measured at each wavelength using an EnergyMax-USB J-10MB energy sensor (Coherent Inc., Santa Clara, CA). The PG142C output beam was focused into the ion trap. The typical experimental setup consisted of electrospraying the peptide solution into the mass spectrometer, isolating the doubly charged ion in the ion trap, and performing ETD at 100−200 ms ion−ion reaction time to produce the desired cation-radical. The fragment cation radical was isolated by mass and subjected to photoactivation from 210−400 nm. The intensities of the resulting UVPD MS^3 photofragments were monitored as a function of wavelength, and their final intensities were normalized to the laser output power to plot the action spectra. The number of laser pulses used during each isolation depended on the photodissociation yield at each given wavelength, and ranged from 1 to 19 pulses, corresponding to 100−1000 ms activation time, respectively, with each successive pulse spaced by 50 ms.

DOI: 10.1021/acs.jpcb.7b04661
J. Phys. Chem. B 2017, 121, 6557−6569

Calculations. Standard ab initio and density functional theory (DFT) calculations were performed with the Gaussian 09 suite of programs.[45] Ion geometries were optimized using the hybrid B3LYP[46,47] functional and the 6-31+G(d,p) basis set in a spin-unrestricted formalism (UB3LYP). Local energy minima and first-order saddle points (transition states) were characterized by harmonic frequency analysis as having the appropriate number of imaginary frequencies (0 and 1, respectively). The B3LYP-optimized geometries of all relevant ions in the Cartesian coordinate format are given in Tables S1–S26 of the Supporting Information. The structures were used for UB3LYP and Møller–Plesset[48] [UMP2(frozen core)] single-point energy calculations with the 6-311++G(2d,p) basis set. The MP2 energies were corrected by annihilation of higher spin states[49,50] to provide spin-projected (PMP2) energies. In other sets of calculations, B3LYP geometries were used as initial guesses for gradient optimizations with the hybrid ωB97X-D[51,52] and M06-2X[53] methods using the 6-31+G(d,p) basis set, and the obtained optimized geometries were used for single-point energy calculations with the 6-311++G(2d,p) basis set. The calculated energies are given in Table S27 (Supporting Information). DFT calculations of peptide ion relative energies using different hybrid functionals have been reported to show a divergent trend.[43] Moreover, hybrid functionals including dispersion interactions are necessary for calculations of ion–molecule complexes. To treat a range of peptide cation-radical structures, transition states, and dissociation products, it is desirable to use a variety of computational methods to obtain consensus and identify outliers.

Potential energy surface mapping was performed by Born–Oppenheimer Molecular Dynamics (BOMD) calculations using the semiempirical PM6 method[54] supplemented with dispersion corrections,[55] PM6-D3H4. These calculations were run by MOPAC[56] under the Cuby4 platform which acts as the high-level interface.[57] The typical MD run involved a total of 100 ps with a 1 fs time step with the thermostat set at 520 K to sample the conformational space of each ion. This corresponded to approximately 180 kJ mol^{-1} internal (rovibrational) energy which was considered sufficient for breaking and reforming hydrogen bonding interactions in the cation radicals. Two thousand five hundred snapshots were obtained and subsequently optimized with PM6-D3H4, and 11–20 best representative structures were treated with DFT as described above. Excited-state calculations were performed using time-dependent DFT[58] with M06-2X, ωB97X-D, and LC-BLYP[59] functionals and the 6-31+G(d,p) basis set. Previous benchmarking of peptide radical excitation energies[60] identified TD-DFT with the ωB97X-D functional as giving the closest match to high-level equation-of-motion CCSD calculations,[61,62] and therefore ωB97X-D was used throughout this work to interpret the experimental data. TD-DFT calculations with the 6-31+G(d,p) and 6-311++G(2d,p) basis sets showed closely similar excitation energies and absorption wavelengths, as illustrated by the root-mean-square deviation for the *trans*-amide $[^{\bullet}ATAR+H]^+$ ion *trans*-**1**, giving rmsd = 2.2 nm for lines in the 200–400 nm region. Therefore, the smaller 6-31+G(d,p) basis set was used throughout for TD-DFT excited-state calculations. Vibronically broadened spectra were generated with Newton-Xspace (version 1.4, www.newtonx.org)[63,64] program. Optimized Cartesian atomic coordinates and harmonic frequencies obtained with B3LYP/6-31+G(d,p) were used to generate random configurations that were weighted according to their Boltzmann factors at 300 K. A total of 12 excited electronic states produced by TD-DFT with ωB97X-D/6-31+G(d,p) and 500 configurations were used to produce the spectrum.

Rice–Ramsperger–Kassel–Marcus (RRKM) calculations[65] were performed using the QCPE program of Zhu and Hase[66] that was recompiled for Windows.[67] Unimolecular rate constants were obtained by direct count of quantum states. Rotational states were treated adiabatically and the RRKM microcanonical rate constants were Boltzmann-averaged for the experimental temperature.

RESULTS AND DISCUSSION

Cation-Radical Formation and Dissociations. The $[z_4+H]^{+\bullet}$ ions corresponding to $[^{\bullet}ATAR+H]^+$ and $[^{\bullet}ATAR\text{-}OCH_3+H]^+$ amino acid sequences (Scheme 1, R= H, CH_3) were generated by the following standard procedure. Doubly protonated peptides, $(AATAR+2H)^{2+}$ and $(AATAR\text{-}OCH_3+2H)^{2+}$, respectively, were produced by electrospray ionization from aqueous-methanol solutions, the ions were mass-selected and stored in the linear quadrupole ion trap. An ion–ion reaction with fluoranthene anions of the trapped peptide dications resulted in electron transfer dissociation forming a series of $[z_n+H]^{+\bullet}$ ions shown in Figure S1a,b (Supporting Information). The $[z_4+H]^{+\bullet}$ ions, *m/z* 402 and *m/z* 416 for $[^{\bullet}ATAR+H]^+$ and $[^{\bullet}ATAR\text{-}OCH_3+H]^+$, respectively, were isolated by mass and further probed by collisional activation and photodissociation. Collision-induced dissociation (CID) of trapped ions proceeds by incremental vibrational excitation which is essentially a thermal process similar to slow heating. Under these slow-heating conditions, $[^{\bullet}ATAR+H]^+$ and $[^{\bullet}ATAR\text{-}OCH_3+H]^+$ cation-radicals underwent competitive dissociations resulting in loss of water (*m/z* 384), $C_3H_6NO^{\bullet}$ (*m/z* 330, $[z_3]^+$), C_3H_7NO (*m/z* 329, $[z_3 - H]^{+\bullet}$), and N–C_α bond cleavage forming the $[z_2+H]^{+\bullet}$ ions (*m/z* 230) (Figure 1a). These appeared with similar relative intensities at *m/z* 398, 344, 343, and 244 for the respective homologous ions from the peptide methyl ester (Figure 1b) and corroborated the fragment ion assignment. The dissociations leading to $[z_2+H]^{+\bullet}$ ions may proceed in two steps, as reported for other $[z_4+H]^{+\bullet}$ ions.[40] For peptide fragment ion nomenclature see ref 26.

Photodissociation (UVPD) of the $[z_4+H]^{+\bullet}$ ions was initially performed at 355 nm which specifically targets the second (B) excited electronic state of the C_α-CO radical chromophore.[42] UVPD resulted in loss of water, $C_3H_6NO^{\bullet}$, and C_3H_7NO neutral fragments that were analogous to those in the CID spectrum. In addition, UVPD induced several dissociations that were absent on CID, namely, loss of OH and backbone cleavages resulting in the formation of C-terminal fragment ions with closed electron shells, $[y_3]^+$, $[y_3 - C_2H_4O]^+$, $[y_2+H]^+$, and $[y_2]^+$ at *m/z* 345, 301, 246, and 244, respectively (Figure 2a), that showed the expected 14 Da homologous mass shifts for the $[z_4+H]^{+\bullet}$ methyl ester ion (Figure 2b). All these fragment ions contain the C-terminal arginine residue. The relevant bond dissociations forming these ions and their sketched structures are shown as insets in Figure 2.

The nature of the major CID fragment ions $[z_3]^+$and $[z_3 - H]^{+\bullet}$, was further investigated by selecting them by mass followed by collisional activation and photodissociation at 355 nm (Figure S2, Supporting Information). CID of both ions resulted in the elimination of a 84 Da neutral ($C_4H_4O_2$) from the Thr residue, forming the $[y_2+H]^{+\bullet}$ (*m/z* 245) and $[y_2+2H]^+$ (*m/z* 246) ions, respectively (Figure S2a,b). Only

DOI: 10.1021/acs.jpcb.7b04661
J. Phys. Chem. B 2017, 121, 6557–6569

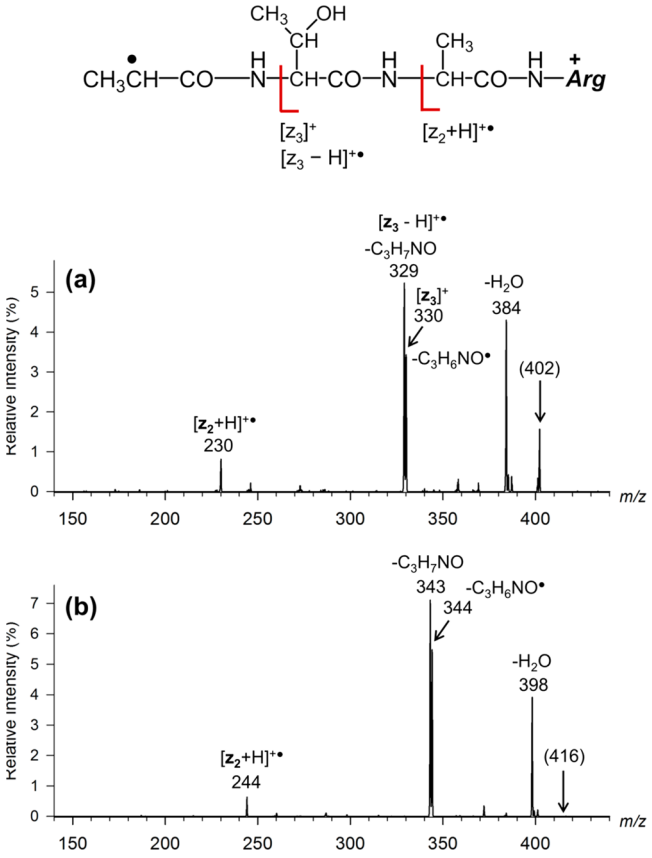

Figure 1. CID of $[z_4+H]^{+\bullet}$ ions generated by ETD of (a) $[AATAR+2H]^{2+}$ and (b) $[AATAR\text{-}OCH_3+2H]^{2+}$.

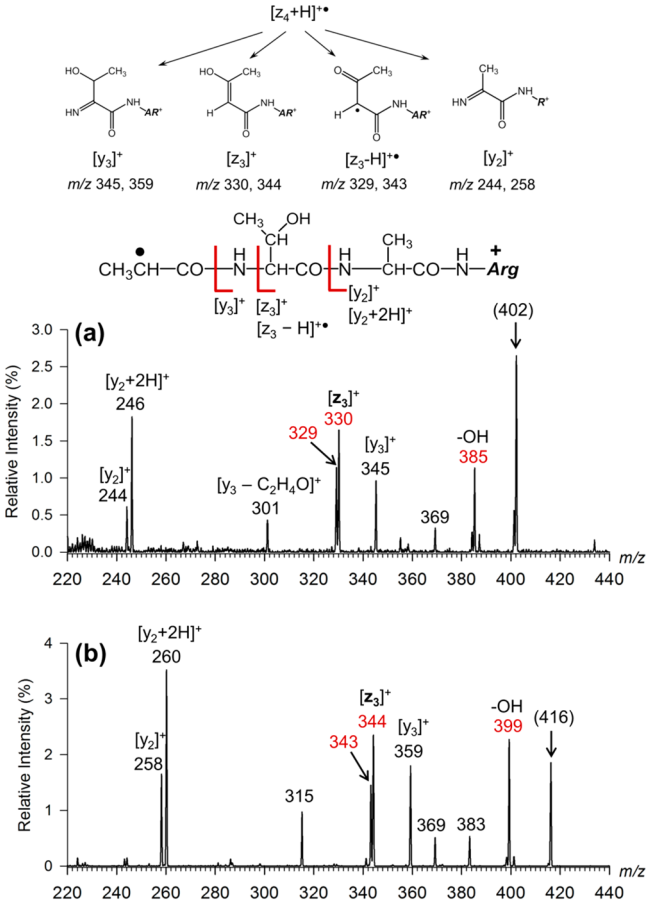

Figure 2. Photodissociation (355 nm, 3 laser pulses) of $[z_4+H]^{+\bullet}$ ions generated by ETD of (a) $[AATAR+2H]^{2+}$ and (b) $[AATAR\text{-}OCH_3+2H]^{2+}$.

the cation-radicals, m/z 329 and m/z 343 from $[^{\bullet}ATAR+H]^+$ and $[^{\bullet}ATAR\text{-}OCH_3+H]^+$, respectively, showed photodissociation, resulting in backbone cleavage between the Thr and Ala residues and formation of $[y_2]^+$ ions at m/z 244 and 258 (Figure S2c). The m/z 330 and 344 even-electron ions did not photodissociate at 355 nm (Figure S2d).

Photodissociation and Action Spectrum of $[z_4+H]^{+\bullet}$ Ions. Before analyzing and discussing the dissociations of the $[z_4+H]^{+\bullet}$ ions, it is desirable to establish their structure. Peptide cation-radicals are known to undergo radical-induced rearrangements by hydrogen migrations[68−78] that can be triggered by internal excitation provided by exothermic electron transfer.[79] To characterize the $[z_4+H]^{+\bullet}$ ions, we first monitored photodissociation of the $[^{\bullet}ATAR+H]^+$ ion at 355 nm as a function of the number of laser pulses. This provided an exponential curve, $I(n) = I_0e^{-0.53n}$, (correlation coefficient: r^2 = 0.996, root-mean-square deviation: rmsd = 2.9%) shown in Figure S3a, where I_0 and $I(n)$ are, respectively, the normalized initial and residual $[z_4+H]^{+\bullet}$ ion intensity after n pulses. The asymptotic decrease to zero of $I(n)$ indicated that all $[z_4+H]^{+\bullet}$ species in the ion population produced by ETD and stored in the ion trap absorbed light at 355 nm and underwent photodissociation upon absorption of the 3.4925 eV (337 kJ mol^{-1}) photon. The homologous $[^{\bullet}ATAR\text{-}OCH_3+H]^+$ ion also showed a single-exponential decay upon irradiation at 355 nm, $I(n) = I_0e^{-0.66n}$, (correlation coefficient: r^2 = 0.992, root-mean-square deviation: rmsd = 2.6%), indicating a close similarity between the $[z_4+H]^{+\bullet}$ ions generated from the peptide and its methyl ester (Figure S3a). The photofragment ion relative intensities increased asymptotically for all even-electron species, as illustrated for ions from $[^{\bullet}ATAR\text{-}OCH_3+H]^+$ (Figure S3b). In contrast, the $[z_4+H-H_2O]^{+\bullet}$ and $[z_3-H]^{+\bullet}$ cation-radical fragment ions reached a maximum and then were depleted upon further laser pulses, indicating that these species photodissociated at 355 nm.

More detailed absorption characteristics of the $[z_4+H]^{+\bullet}$ ions were obtained from the UVPD action spectrum (Figure 3a,b). The mass-resolved fragment ion channels (Figure 3a) showed two prominent broad absorption maxima at 360 and 225 nm that are visualized by the overall action spectrum, constructed as a sum of normalized photofragment ion intensities at 210−400 nm from all monitored channels (Figure 3b). The major dissociation channels showed different absorption characteristics along the wavelength axis. In particular, the m/z 384 fragment ion by loss of H_2O peaked at 360 nm but relatively decreased at 230 nm. This could be due to consecutive dissociations of this radical fragment ion following absorption of a high energy photon. In contrast, the m/z 385 closed-shell fragment ion by loss of OH dominated at 230 nm, possibly because of its stability. The $[z_3]^+$ (m/z 330) and $[y_3]^+$ (m/z 345) channels showed maxima in both the 340−360 and 220−230 nm regions. The low-mass channels of the $[y_2]^+$ and $[y_2+2H]^+$ fragment ions could not be monitored across the entire wavelength region because of interference from background ions from photodesorbed fluoranthene.[21] The interpretation of the action spectrum (Figure 3c) and structure assignment for the $[z_4+H]^{+\bullet}$ ions required extensive calculations that are described in the next section.

DOI: 10.1021/acs.jpcb.7b04661
J. Phys. Chem. B 2017, 121, 6557−6569

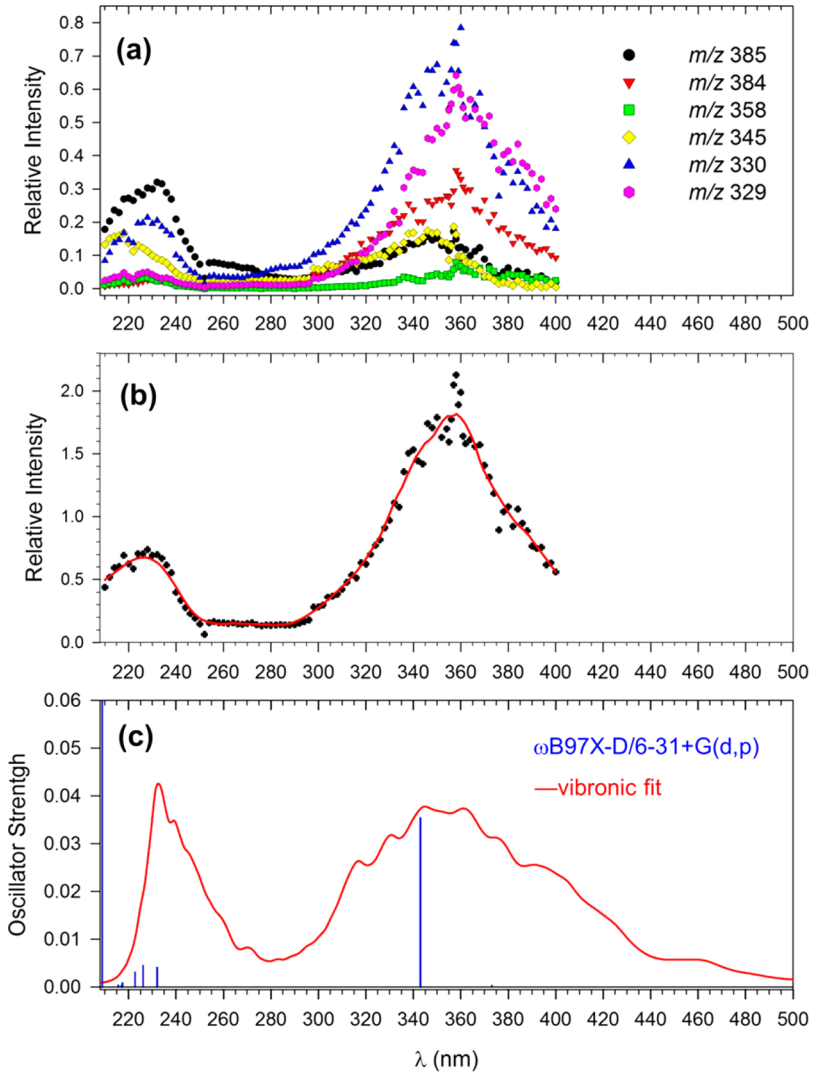

Figure 3. Photodissociation action spectrum of $[^{\bullet}ATAR+H]^+$ ion. (a) Mass-channel resolved spectra: the *m*/*z* 385, 384, 358, 345, 330, and 329 channels correspond to losses of OH, H_2O, C_2H_4O, C_3H_5O, C_3H_6NO, and C_3H_7NO, respectively. (b) Overall action spectrum from the sum of photofragment ion relative intensities. (c) Calculated vibronic absorption spectrum at 300 K of *trans*-**1**. For ion structure see Figure 4.

Ion Structures. Investigations of peptide cation-radical structures involve three major features: (1) charge location, (2) radical site location, and (3) peptide conformation. With $[^{\bullet}ATAR+H]^+$, the charge is firmly sequestered by protonation of the basic Arg residue (Scheme 1). The radical site can migrate from the former *N*-terminal C_α (C-14) to backbone C_α positions at Thr (C-3), Ala (C-9), or Arg (C-18), or to the C_β position in the Thr residue (C-6, for atom numbering see Scheme 1). All these radicals (*trans*-**2**−**5**, Figure 4) are expected to be low-energy isomers of the initial *N*-terminal C_α structure *trans*-**1**.[21] An isomer with the radical site in the Arg side chain (**6**, Figure 4) was found to be substantially destabilized against *trans*-**1**-**5** and is not likely to be formed by ETD. Analysis of the radical position and ion conformation in $[^{\bullet}ATAR+H]^+$ followed a multistep procedure aimed at capturing both the local energy minima and the connecting transition states as first-order saddle points. The initial $[^{\bullet}ATAR+H]^+$ structure was built from the homologous serine-containing $[z_4+H]^{+\bullet}$ ion, $[^{\bullet}ASAR+H]^+$,[42] and optimized with B3LYP. The optimized structure was subjected to BOMD/PM6-D3H4 for 100 ps at 520 K, 2500 snapshots were extracted and optimized by PM6-D3H4. From these, 20 low-energy structures within a 20 kJ mol^{-1} energy range were obtained and fully reoptimized with DFT. The lowest-energy ion (*trans*-**1**) is shown in Figure 4. B3LYP, ωB97X-D/6-31+G(d,p), and M06-2X geometry optimizations yielded very similar lowest-energy ion structures that are represented by *trans*-**1**.

Ion structures in which the radical site migrated to another position were obtained according to the following procedure. Starting with *trans*-**1**, the *N*-terminal amide bond was rotated through **TS1** from the trans to a cis configuration and the resulting *cis*-isomer (*cis*-**1**) was used to search for the transition state (**TS2**) for the Thr alpha H atom migration from C-3 to the *N*-terminal radical site (C-14) using B3LYP. Note that the amide rotation is necessary to make the alpha and beta hydrogen atoms sterically accessible for transfer through respective five- and six-membered membered cyclic transition states. The critical parameters of the **TS2** geometry, which are the lengths of the forming C-14−H and breaking C-3−H bonds, were constrained while the other atoms were fully dynamic in the subsequent BOMD/PM6-D3H4 trajectory calculations that were run for 100 ps at 520 K. Eleven lowest-energy structures were extracted and fully optimized to the first-order saddle points with B3LYP, ωB97X-D, and M06-2X to

DOI: 10.1021/acs.jpcb.7b04661
J. Phys. Chem. B 2017, 121, 6557−6569

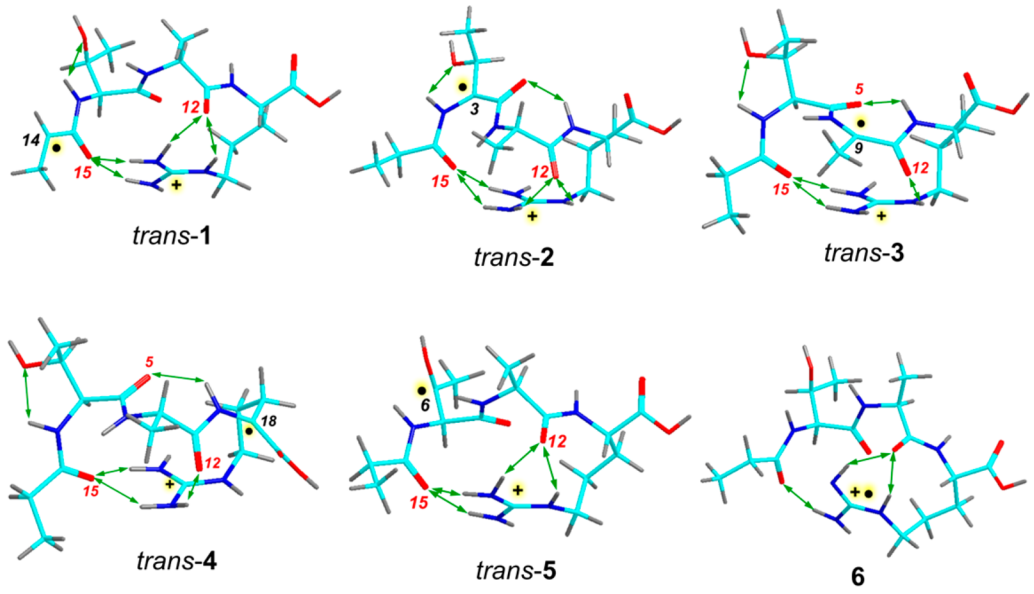

Figure 4. ωB97X-D/6-31+G(d,p) optimized structures of *trans*-**1**−**6**. Green arrows indicate major hydrogen bonds of d(X—H) < 2.2 Å. For ion relative energies see Table 1.

obtain new TS geometries. The lowest-energy TS was selected for intrinsic reaction coordinate (IRC)[80] search to find the structure of the *cis*-**1** reactant and the H-migration product, which was a *cis*-amide (*cis*-**2**). Both ions were fully optimized by DFT to give the final structures (Figure S4, Supporting Information). This procedure preserves the structural continuity for the *cis*-**1** → **TS2** → *cis*-**2** reaction while providing an electronically and conformationally optimized TS structure for the further analysis of the potential energy surface (*vide infra*). Amide rotation in *cis*-**2** through **TS3** then produced the more stable trans-amide isomer that was subjected to BOMD/PM6-D3H4 run, and 12 lowest-energy structures were fully optimized with DFT to yield *trans*-**2** (Figure 4). The calculations indicated that the hydrogen bonding pattern in *trans*-**1** and *trans*-**2** was conserved, showing internal solvation of the Arg guanidinium ion by the O-15 and O-12 amide carbonyls (Figure 4). Based on this finding, the Ala (C-9) and Arg (C-18) radicals were built from *trans*-**2** and fully optimized by DFT without the BOMD conformational run, yielding radicals *trans*-**3** and *trans*-**4** (Figure 4). In contrast, the hydrogen bonding pattern of the Thr hydroxyl depended on the amide *cis*-*trans* geometry and, therefore, the C-6 beta radical (*trans*-**5**, Figure 4) was generated by a procedure analogous to that employed for *trans*-**2**. Briefly, a TS for the beta H transfer in *cis*-**1** was found by combined DFT/BOMD/DFT (**TS4**) and the *cis*-**5** isomer was obtained by IRC from **TS4** followed by BOMD/DFT optimization (Figure S4, Supporting Information). The trans isomer (*trans*-**5**) was obtained after amide rotation through **TS5**, followed by BOMD/DFT optimization. The *trans*-amide radicals **1**−**5** showed very similar 0 K energies relative to *trans*-**1** that was used as a reference (E_{rel} = 0.0 kJ mol^{-1}, Table 1).

Action Spectrum Assignment. To interpret and assign the bands in the UVPD action spectrum of the $[z_4+H]^{+\bullet}$ ion, we performed TD-DFT calculations of excitation energies and oscillator strengths of *trans*-isomers **1**−**5**, and also the pertinent *cis*-amide isomers. Ion *trans*-**1** showed major transitions at 343 and 209 nm, several minor ones between 220 and 240 nm, and a very weak band at 374 nm, all based on ωB97X-D TD-DFT calculations (Figure 5a). Calculations with the other DFT functionals (M06-2X and LC-BLYP) gave similar absorption patterns for *trans*-**1**, showing wavelength shifts of the calculated lines, as summarized in Table S28 (Supporting Information). In particular, the LC-BLYP excitation energies were blue-shifted relative to those from ωB97X-D and M06-2X, consistent with the results of a previous benchmarking study.[60] The electron transitions leading to the five lowest excited states in *trans*-**1** are listed in Table S29 (Supporting Information). The prominent band at 343 nm includes excitations from lower β molecular orbitals to the lowest unoccupied MO108β of a π_z type, which is delocalized over the CH_3−$CH^{\bullet}$-CO-NH moiety (Table S29).

Radicals *trans*-**2**−**5** showed distinctly different absorption spectra (Figure 5b,c). The calculated spectrum of *trans*-**2** showed weak bands at 358 and 377 nm whereas the major bands appeared at 302, 260, 245, and 244 nm (Figure 5b). The Ala-C_α radical *trans*-**3** displayed a weak absorption band at 341 nm and stronger ones at 313, 250, and 233 nm (Figure 5c). The Arg-C_α radical *trans*-**4** had a weak band at 316 nm and strong ones at 276 and 232 nm with further moderately strong bands at 228, 222, and 218 nm (Figure 5c). The Thr-C_β radical *trans*-**5** showed the longest wavelength absorption at 287 nm and several moderately strong bands at 250, 243, and 211 nm (Figure 5b). For a complete list of transitions cf. Table S28 (Supporting Information).

The calculated absorption spectra of *trans*-**1**−**5** were compared with the photodissociation action spectrum of the $[z_4+H]^{+\bullet}$ ion. The latter did not display absorption bands in the 250−300 nm region that would be expected if isomers *trans*-**2**−**5** were present. In contrast, the action spectrum was consistent with the calculated absorption spectrum of *trans*-**1**. This similarity was further corroborated by comparing the action spectrum with the vibronically broadened absorption spectrum of *trans*-**1** that showed a close match of the band shapes and λ_{max}. The calculated absorption spectra of the *cis*-amide isomers, *cis*-**1**, **2**, and **5**, showed patterns that were similar to those for the corresponding *trans*-amide isomers, but displayed red shifts for the long wavelength bands (Figure 5d). In summary, the photodissociation action spectrum of the $[z_4+H]^{+\bullet}$ ion

DOI: 10.1021/acs.jpcb.7b04661
J. Phys. Chem. B 2017, 121, 6557−6569

Table 1. Relative Energies of $[^{\bullet}ATAR+H]^+$ Cation Radicals

ion	relative energy[a,b]			
	B3LYP[c]	ωB97X-D[c]	M06-2X[c]	PMP2[c,d]
trans-**1**	0	0	0	0
trans-**2**	0.4	2.4	5.5	7.9
trans-**3**	15	6.7	6.7	11
trans-**4**	−11	−10	−11	−13
trans-**5**	3.2	3.5	7.7	6.9
6	96	94	94	93
cis-**1**	15	14	18	20
cis-**2**	24	16	24	35
cis-**5**	51	33	41	50
TS1	55	58	45	61
TS2	125	119	130	112
TS3	66	71	71	75
TS4	117	100	113	107
TS5	58	60	57	62
TS6	91	115	126	136
TS7	84	108	106	108
TS8	125	143	151	168
TS9	128	145	144	158
7	57	93	99	119
8	−44	−7	−3	16
9	−71	−43	−31	−21
10a	20	72	73	78
10b	−13	31	40	39
11a	119	120	122	144
11g	−49	−34	−31	-[e]
12	102	139	118	122
$[z_3]^+ + C_3H_6NO^{\bullet}$	21	75	79	81
$[z_3 - H]^{+\bullet} + C_3H_7NO$	−5	41	53	63
$[x_2+H]^{+\bullet} + a_2$	65	122	129	127
$[z_4+H - OH]^+ + OH^{\bullet}$	138	159	166	160
$[z_4+H - H_2O]^{+\bullet} + H_2O$	−1	27	36	5
$[y_3]^+ + CH_3CH_2CO^{\bullet}$	129	164	163	165

[a]In kJ mol^{-1}. [b]Including B3LYP/6-31+G(d,p) zero-point energy corrections with frequencies scaled by 0.975 and referring to 0 K. [c]From single-point energy calculations with the 6-311++G(2d,p) basis set. [d]Spin-corrected values. [e]MP2 calculations failed.

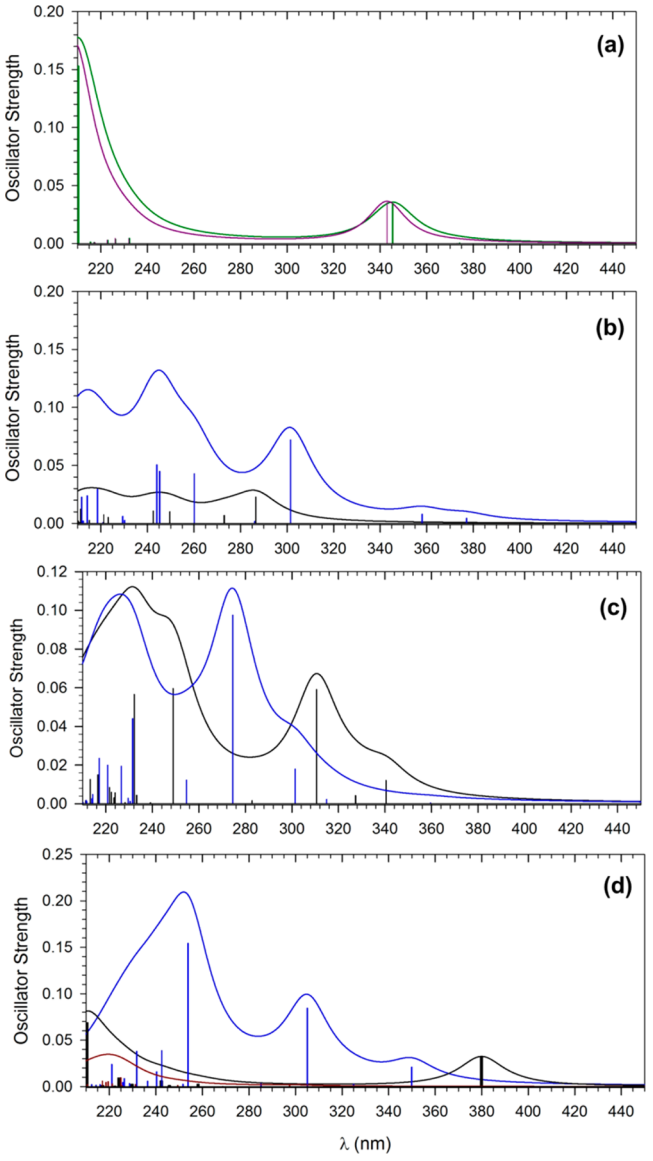

Figure 5. TD-DFT ωB97X-D absorption spectra of (a) *trans*-**1** (purple: calculations with the 6-31+G(d,p) basis set; green: calculations with the 6-311++G(2d,p) basis set); (b) blue: *trans*-**2**, black: *trans*-**5**; (c) black: *trans*-**3**; blue: *trans*-**4**; (d) blue: *cis*-**2**; black: *cis*-**1**; purple: *cis*-**5**.

generated by ETD very well matches the calculated absorption spectrum of *trans*-**1** (Figure 3c). This is the expected structure to be formed by dissociation of the N−C_α bond between the Ala and Thr residues in the $(AATAR+2H)^{+\bullet}$ cation-radical. Conversely, the assigned structure provides evidence that, under the ETD conditions, the $[z_4+H]^{+\bullet}$ ions did not undergo isomerization by hydrogen migrations.

The kinetic stability of $[^{\bullet}ATAR+H]^+$ contrasts the behavior of the related cation radicals $[^{\bullet}AFAR+H]^+$, $[^{\bullet}AWAR+H]^+$ (ref 21), $[^{\bullet}FAR+H]^+$, and $[^{\bullet}DAR+H]^+$ that have been found to isomerize by hydrogen migrations when formed by ETD.[38] The related $[^{\bullet}AHAR+H]^+$ ion has been reported to retain the canonical structure on the basis of an IRMPD action spectrum.[20] We note that analysis of UVPD spectra of $[^{\bullet}AHAR+H]^+$ revealed ca. 6% isomers other than the canonical structure.[38] The structural integrity of $[^{\bullet}ATAR+H]^+$ is not obviously related to the isomerization thermodynamics. The isomeric radicals *trans*-**2** and *trans*-**5** have energies very similar to that of *trans*-**1**, whereas *trans*-**3** and *trans*-**4** are even more stable. The reason for the stability of $[^{\bullet}ATAR+H]^+$ and different behavior of peptide cation radicals carrying different amino acid residues may be found in the isomerization kinetics and relative stabilities of the intermediates.[21] Isomerization and dissociation mechanisms of $[^{\bullet}ATAR+H]^+$ are addressed in the next section.

Isomerization and Dissociation Pathways. In this section we present and discuss the energetics of $[z_4+H]^{+\bullet}$ ion isomerizations and dissociations. The $[z_4+H]^{+\bullet}$ ions showed four major dissociations upon collisional activation in the slow-heating regime: loss of H_2O, $C_3H_6NO^{\bullet}$, C_3H_7NO, and formation of the $[z_2+H]^{+\bullet}$ ions. All these dissociations require hydrogen atom migrations to produce intermediates from which the neutral fragments are formed. Since action spectroscopy pointed to *trans*-**1** as the dominant $[z_4+H]^{+\bullet}$ ion species formed by ETD, our investigations of the potential energy surface for isomerizations and dissociations started with this structure. The relative energies from ωB97X-D/6-311++G(2d,p) calculations that include zero-point energy corrections are plotted in a comprehensive potential energy diagram

DOI: 10.1021/acs.jpcb.7b04661
J. Phys. Chem. B 2017, 121, 6557−6569

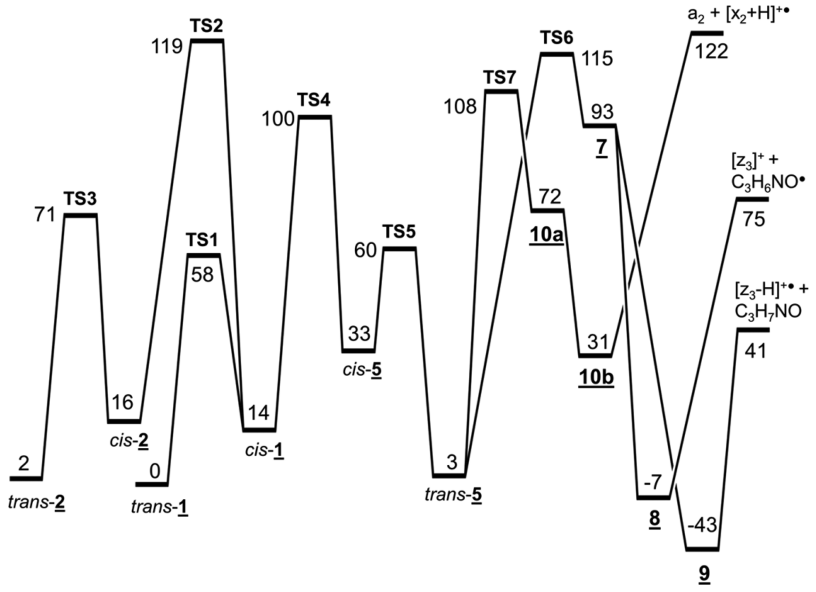

Figure 6. Potential energy diagram of ωB97X-D/6-311++G(2d,p) relative energies (kJ mol^{-1}) including zero-point corrections. **TS1**: amide rotation; **TS2**: Thr-H_α transfer; **TS3**: amide rotation; **TS4**: Thr-H_β transfer; **TS5**: amide rotation; **TS6**: N−C_α bond dissociation; **TS7**: C_α—CO bond dissociation.

(Figure 6). Relative energies were also obtained by MP2, and M06-2X single-point calculations, as compiled in Table 1. The ωB97X-D, MP2, and M06-2X data largely agree in ranking the ion relative energies across the entire set. The B3LYP calculations overestimate the stabilities of several ion−molecule complexes relative to the bound structures and dissociation products.

The $C_3H_6NO^\bullet$ and C_3H_7NO neutral fragments logically originate from the deaminated *N*-terminal Ala residue by cleavage of the N−C_α bond at Thr. By stoichiometry, the neutral fragments must pick up one or two hydrogen atoms, respectively, in the course of dissociation. The N−C_α bond dissociation indicates activation by an adjacent radical. These features led to the proposed reaction sequence (Scheme 2) which starts with *trans-cis* amide rotation in *trans*-**1** through a low-energy **TS1**, forming *cis*-**1**. Migration of the beta hydrogen from the Thr side chain in *cis*-**1** through **TS4** forms intermediate *cis*-**5** which can stabilize by amide rotation through **TS5** to form *trans*-**5**. N−C_α bond cleavage in *trans*-**5** via **TS6** forms a complex (**7**) of the incipient $C_3H_6NO^\bullet$ radical and the $[z_3]^+$ product ion (Figure S5, Supporting Information). Complex **7** can undergo stabilizing isomerizations before the products separate. Thus, prototropic isomerization of the $C_3H_6NO^\bullet$ moiety to a more stable C_α-radical can form the lower-energy complex **8**. Further isomerization by hydrogen transfer can form a low-energy complex of the $[z_3-H]^{+\bullet}$ ion with propionamide (**9**). The dissociation thresholds for loss of $C_3H_6NO^\bullet$ from **8** (82 kJ mol^{-1}) and loss of C_3H_7NO from **9** (84 kJ mol^{-1}) are well below the **TS6** energy (122 and 158 kJ mol^{-1} relative to **8** and **9**, respectively), indicating that the dissociations proceeding through **TS6** are not reversible.

The assumption of a common rate-determining step (**TS6**) and intermediate (**7**) for the loss of $C_3H_6NO^\bullet$ and C_3H_7NO is consistent with the relatively weak dependence on ion internal energy of the branching ratio for these dissociations, expressed as the product ion intensity ratio [*m*/*z* 330]/[*m*/*z* 329]. Vibrational excitation by collisional activation gave [*m*/*z* 330]/[*m*/*z* 329] = 0.67 from [$^\bullet$ATAR+H^+] and [*m*/*z* 344]/[*m*/*z* 343] = 0.78 for the homologous [$^\bullet$ATAR-OCH_3+H^+]. Upon higher-energy photoexcitation these ratios shift to 0.95 and 1.02, respectively, equally favoring the C_3H_7NO and $C_3H_6NO^\bullet$ loss. This can be explained by energy-dependent competition between fragment separation in **7**. This can proceed through a

Scheme 2. Proposed Reaction Sequence Leading to the Formation of $[z_3]^+$ and $[z_3 - H]^{+\bullet}$ Ions[a]

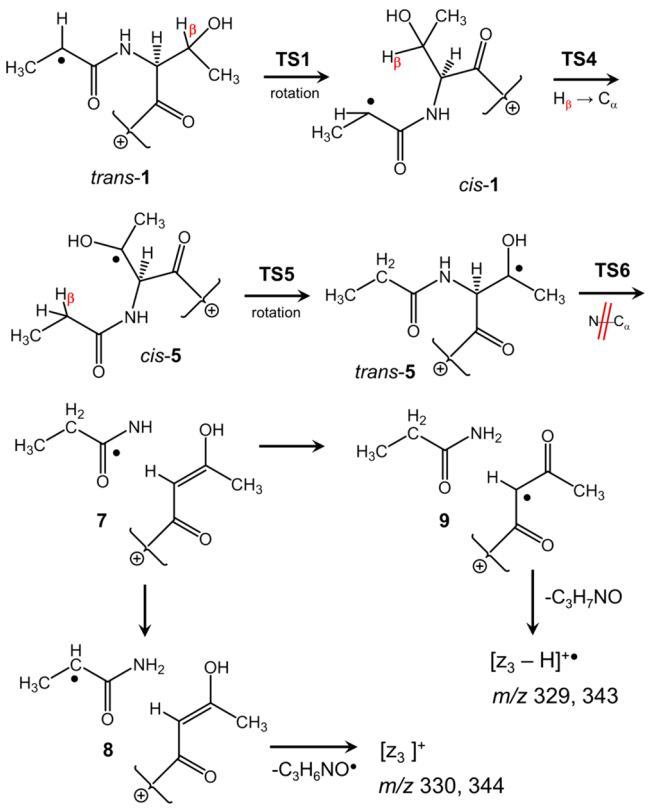

[a]For fully optimized structures see Figure S5 (Supporting Information).

DOI: 10.1021/acs.jpcb.7b04661
J. Phys. Chem. B 2017, 121, 6557−6569

loose transition state for loss of $C_3H_6NO^{\bullet}$ which is preferred at higher internal energies, or a hydrogen migration (tight transition state) forming $CH_3CH_2CONH_2$ in the very stable complex **9**, which is expected to be competitive at internal energies closer to **TS6**. It should be noted, however, that the dissociation kinetics are expected to be affected by substantial kinetic shifts,[81,82] requiring excess energy for the reaction to proceed on the experimental time scale. RRKM calculations of rate constants (Figure S6) indicate a 110 kJ mol^{-1} kinetic shift for 50% conversion of *trans*-**1** via **TS6** at 30 ms which is comparable to the experimental time scale for the dissociations. The mean energy in photoexcited *trans*-**1** is composed of the ion 310 K ro-vibrational enthalpy (80 kJ mol^{-1}) and the 355 nm photon energy to give E = 80 + 337 = 417 kJ mol^{-1} which substantially exceeds the energy needed to proceed through **TS6** even considering the kinetic shift.

The Thr beta radical *trans*-**5** can also represent an intermediate for the formation of the $[z_2+H]^{+\bullet}$ fragment ion observed in the CID spectrum. In the proposed reaction sequence (Scheme 3), radical-promoted cleavage of the

Scheme 3. Proposed Reaction Scheme Leading to the Formation of $[z_2+H]^{+\bullet}$ Ions

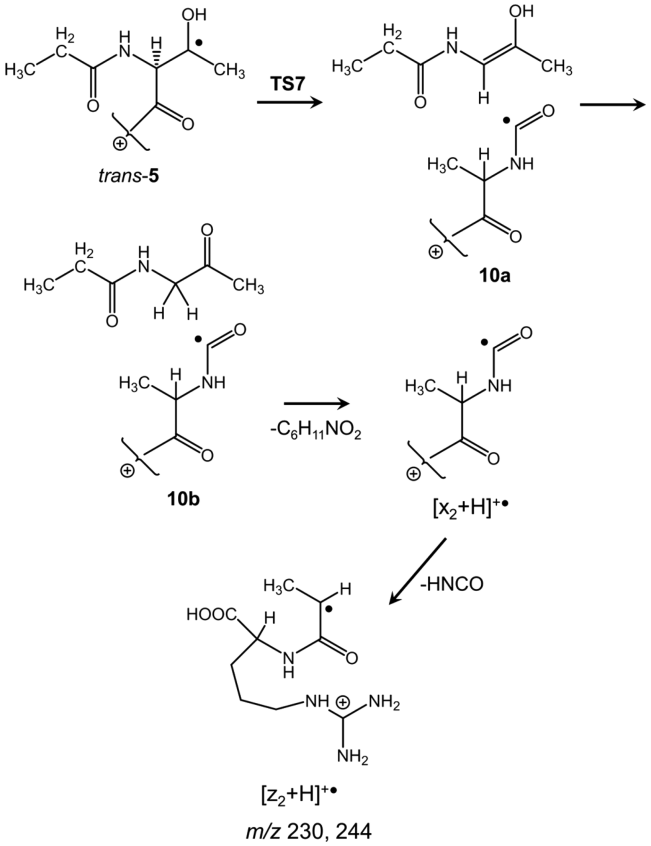

adjacent C_α–CO bond can proceed via **TS7**, forming a complex of the incipient a_2 and $[x_2+H]^{+\bullet}$ fragments (**10a**). The a_2 molecule can undergo a stabilizing prototropic rearrangement (**10b**) that lowers the dissociation threshold for the formation of the $[x_2+H]^{+\bullet}$ ion. This ion spontaneously dissociates by loss of HNCO[40] to form the $[z_2+H]^{+\bullet}$ ion.

Born–Oppenheimer Molecular Dynamics of Water Complexes. The role of ion–molecule complexes is further emphasized by the analysis of the dissociation pathways for the elimination of water from the Thr side chain, which is one of the major CID processes of $[^{\bullet}ATAR+H]^+$ and $[^{\bullet}ATAR-OCH3+H]^+$ ions, accounting respectively for 23 and 22% of the total fragment ion intensity. We note that the side-chain hydroxyl, such as in Ser and Thr, substantially promotes loss of water from $[z_4+H]^{+\bullet}$ ions; in the absence of a side-chain OH the loss of water accounts for only 0.1–4.7% for various amino acid residues.[37]

Upon UVPD, the loss of water from $[^{\bullet}ATAR+H]^+$ competes with the loss of the side-chain OH radical, which indicates a common transition state for these dissociations involving cleavage of the threonine C–OH bond. We considered that dissociation of the C–OH bond can be promoted in the C_α radical *trans*-**2** which is accessible from *trans*-**1** via **TS2** and **TS3** (Figure 6). In the TS for the OH loss (**TS8**) the C_β–OH bond is almost interrupted at 2.444 Å, and the OH radical is hydrogen bonded to the Arg guanidinium cation. The further development along the reaction pathway depends on the ion internal energy. At high energies accessed by photon absorption, the OH radical departs forming the $[z_4+H-OH]^+$ fragment ions. At lower excitations accessed by collisional activation, the OH radical abstracts a hydrogen atom from the $[z_4+H-OH]^+$ ion and departs as a water molecule.

The search for a transition state for water elimination is difficult because of multiple hydrogen-bonding interactions between the polar counterparts that can lead to many possible transition states. We therefore resorted to a BOMD analysis that was performed with nine reaction trajectories starting with a complex (**11a**) accessed from **TS8**. The general feature of these trajectories was an early abstraction of a guanidinium hydrogen (H-52, Scheme 4) by the OH radical, (O-7–H-54, Scheme 4), forming a water complex with the $[z_4+H-H_2O]^+$ ion. The further development of the water complex differed among the trajectories, but several included a transfer of a hydrogen atom from the Thr methyl group. To illustrate a possible reaction sequence leading to loss of water, we plot one trajectory showing the development of interactions of the hydroxyl O-7 and H-54 atoms with several atoms in the $[z_4+H-OH]^+$ counterpart. In the course of 200 fs, the OH radical captures the H-bonding Arg hydrogen atom (H-52) forming a water complex with a guanidine cation radical (**11b**, Scheme 4). This is shown in Figure 7 as a crossing of the O-7–H-52 (red) and N-28–H-52 (green) trajectories at 200 fs.

At 600 fs, complex **11b** undergoes electron transfer to the guanidine group, ionizing the Thr ene-amide group (**11c**). Intramolecular electron transfer was indicated by ωB97X-D/6-31+G(d,p) population analysis of several snapshots on the trajectory at 575–590 fs that showed ~95% spin density accumulation in the Thr residue, chiefly at the C_α and C_β atoms. This intramolecular red-ox reaction is only slightly endothermic, as deduced from the calculated ionization energies of ethylguanidines (7.75–8.09 eV) and the ene-amide fragment (8.27 eV, Table S30, Supporting Information) and can be promoted by the thermal energy of the complex. The electron transfer is followed by rotation about the enamide double bond (**11d**) and transfer of H-57 from the Thr methyl to the amide O-5 (**11e**). This is shown in Figure 7 by the collapse of the O-5–H-57 (purple) trajectory to within 1 Å at 600 fs. In the subsequent development, the water molecule reorients itself, forming complex **11f** developing H-bonds to H-54 and the guanidine N-28. This is shown in Figure 7 by the N-28–H-54 bond distance (turquoise trajectory) oscillating between 1.6 and 3.4 Å. This configuration lasts until about

DOI: 10.1021/acs.jpcb.7b04661
J. Phys. Chem. B 2017, 121, 6557–6569

Scheme 4. Snapshot Structures of Critical Points Along a Selected BOMD Trajectory for Loss of Water

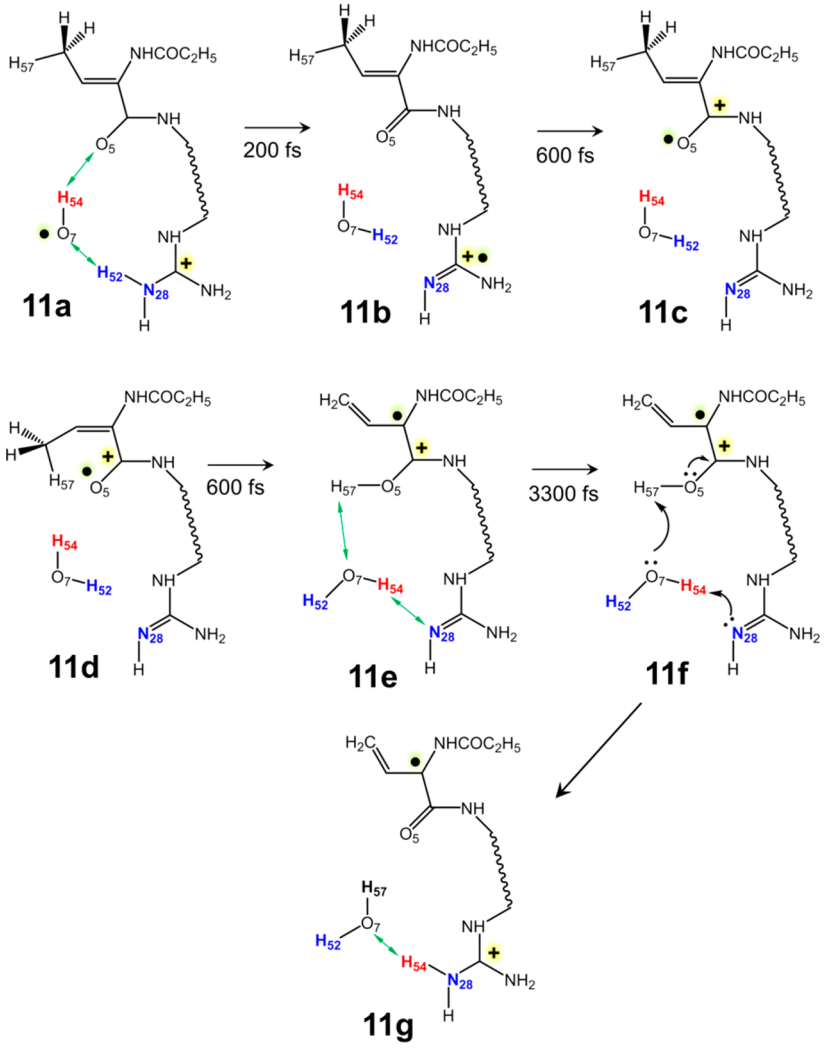

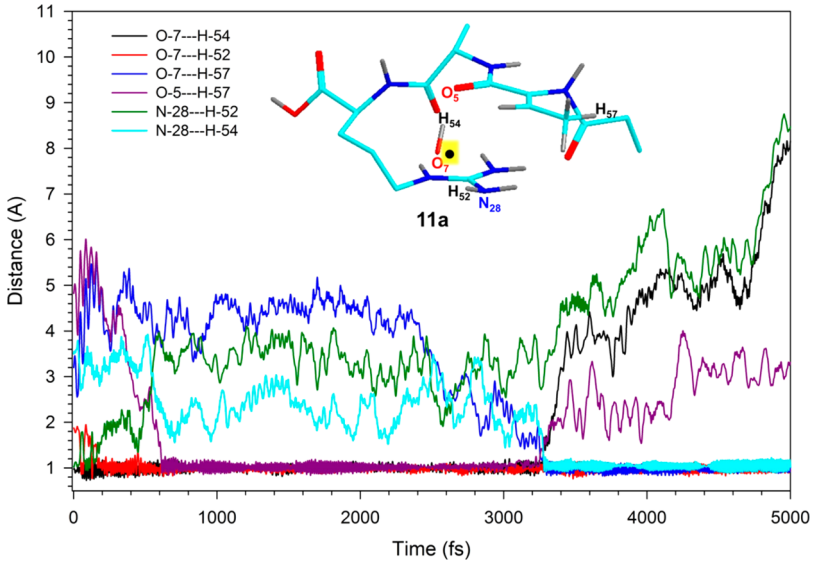

Figure 7. PM6-D3H4 BOMD trajectory analysis of N−H and O−H atomic distances in complexes **11a−g**.

3.2 ps when a very fast tandem proton transfer occurs moving H-57 to O-7 (blue curve) and H-54 to N-28 (crossing of the black and turquoise curves) and forming another complex (**11g**). Thus, in the course of 3 ps, the O-7 atom in the water molecule interacts with several protons, including the initially exchangeable (H-52, H-54) and nonexchangeable (H-57)

DOI: 10.1021/acs.jpcb.7b04661
J. Phys. Chem. B 2017, 121, 6557−6569

hydrogen atoms, and resulting in isomerizations in the remote parts of the complex. The intricate trajectory in complexes **11a−g** is a result of a stepwise exothermic isomerization which is counterbalanced by the substantial water binding energy (61 kJ mol^{-1} in **11b−g**) that delays immediate dissociation.

The C_α radical *trans*-**2** can be considered as an intermediate for another dissociation pathway leading to the $[y_3]^+$ fragment ion which is realized upon UVPD but not CID. Scheme 5 shows cleavage of the CO−NH bond in *trans*-**2** proceeding through **TS9** and forming intermediate complex **12** at 139 kJ mol^{-1} relative to *trans*-**1**. Fragment separation in **12** is asymptotically endothermic, leading to the loss of $CH_3CH_2CO^\bullet$ and formation of the $[y_3]^+$ ion with a threshold energy of 164 kJ mol^{-1} relative to *trans*-**1** (Table 1). The relatively high dissociation threshold for the formation of $[y_3]^+$ may explain why the dissociation is not competitive under CID conditions. However, it can also be argued that the photodissociative loss of $CH_3CH_2CO^\bullet$ proceeds on the potential energy surface of the excited electronic state where the formation of *trans*-**2** can be avoided.[38]

Scheme 5. Proposed Reaction Scheme Leading to the Formation of $[y_3]^+$ Ions

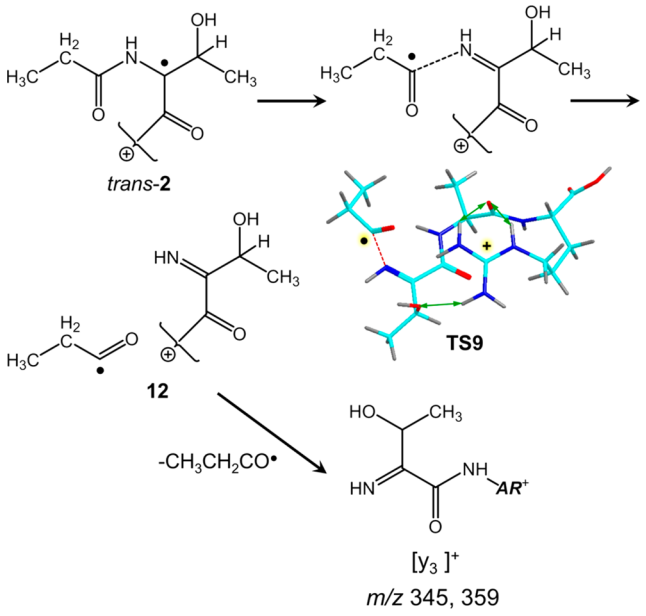

CONCLUSIONS

UV−vis photodissociation action spectroscopy provides unequivocal evidence that the $[^\bullet$Ala-Thr-Ala-Arg+H$]^+$ ion formed by electron transfer dissociation retains its canonical structure in which the radical defect is at the deaminated Ala N-terminus. This finding contributes to our understanding of $[z_n$+H$]^{+\bullet}$ ions structure and stability when formed by exothermic electron transfer dissociation. Extensive TD-DFT calculations of $[z_4$+H$]^{+\bullet}$ ion isomers indicated that the radical position in the peptide ion affects the absorption spectra to allow one to identify the radical isomers. This conclusion is further corroborated by TD-DFT calculations that include vibronic band broadening, leading to improved fit with experimental action spectra. The combination of Born−Oppenheimer molecular dynamics, DFT gradient optimization, and intrinsic reaction coordinate search has been applied for the first time to analyze the potential energy surface of an open-shell peptide ion. This approach holds a tremendous potential in providing potential energy surfaces of improved quality that can be used for calculations of absolute rate constants for peptide radical reactions.

ASSOCIATED CONTENT

Supporting Information

The Supporting Information is available free of charge on the ACS Publications website at DOI: 10.1021/acs.jpcb.7b04661.

Complete refs 26 and 45, B3LYP/6-31+G(d,p) optimized geometries, calculated total and zero-point energies, excitation wavelengths and oscillator strengths of [ATAR+H]+$^\bullet$ cation radicals, Electronic transitions in [$^\bullet$ATAR+H]+ ion *trans*-**1**, structures and ionization energies of guanidine and ene-amine fragments, ETD mass spectra, CID mass spectra, laser pulse dependence, ωB97X-D/6-31+G(d,p) optimized structures, and internal energy dependent molar fractions (PDF)

AUTHOR INFORMATION

Corresponding Author

*E-mail: turecek@chem.washington.edu; Phone 206-685-2041; Fax: 206-685-8665.

ORCID

Prokopis C. Andrikopoulos: 0000-0003-0255-1108

František Tureček: 0000-0001-7321-7858

Author Contributions

§H.T.H. Nguyen and P.C. Andrikopoulos contributed equally to this work and both should be considered as first authors.

Notes

The authors declare no competing financial interest.

ACKNOWLEDGMENTS

Research at University of Washington has received support from the Chemistry Division of the National Science Foundation, Grant CHE-1359810. F.T. thanks Klaus and Mary Ann Saegebarth Endowment for support. Research at the IOCB Prague, was supported by the Grant Agency of the Czech Republic (grant 17-24155S).

REFERENCES

(1) Voicescu, M.; El Khoury, Y.; Martel, D.; Heinrich, M.; Hellwig, P. Spectroscopic Analysis of Tyrosine Derivatives: On the Role of the Tyrosinehistidine Covalent Linkage in Cytochrome c Oxidase. *J. Phys. Chem. B* **2009**, *113*, 13429−13436.

(2) Sjoberg, B. M.; Reichard, P. Nature of the Free Radical in Ribonucleotide Reductase from Escherichia coli. *J. Biol. Chem.* **1977**, *252*, 536−541.

(3) Knappe, J.; Sawers, G. A Radical-Chemical Route to Acetyl-CoA: The Anaerobically Induced Pyruvate Formate-Lyase System of Escherichia coli. *FEMS Microbiol. Rev.* **1990**, *75*, 383−398.

(4) Sawers, G.; Watson, G. A Glycyl Radical Solution: Oxygen-Dependent Interconversion of Pyruvate Formate-Lyase. *Mol. Microbiol.* **1998**, *29*, 945−954.

(5) Whittaker, M. M.; DeVito, V. L.; Asher, S. A.; Whittaker, J. W. Resonance Raman Evidence for Tyrosine Involvement in the Radical Site of Galactose Oxidase. *J. Biol. Chem.* **1989**, *264*, 7104−7106.

(6) Ulas, G.; Lemmin, T.; Wu, Y.; Gassner, G. T.; DeGrado, W. F. Designed Metalloprotein Stabilizes a Semiquinone radical. *Nat. Chem.* **2016**, *8*, 354−359.

(7) Moore, G. F.; Hambourger, M.; Gervaldo, M.; Poluektov, O. G.; Rajh, T.; Gust, D.; Moore, T. A.; Moore, A. L. A Bioinspired Construct

That Mimics the Proton Coupled Electron Transfer Between P680●+ and the TyrZ-His190 Pair of Photosystem II. *J. Am. Chem. Soc.* **2008**, *130*, 10466−10467.
(8) Stubbe, J.; van der Donk, W. A. Protein Radicals in Enzyme Catalysis. *Chem. Rev.* **1998**, *98*, 705−762.
(9) Levin, B. J.; Huang, Y. Y.; Peck, S. C.; Wei, Y.; Martinez-del Campo, A.; Marks, J. A.; Franzosa, E. A.; Huttenhower, C.; Balskus, E. P. A Prominent Glycyl Radical Enzyme in Human Gut Microbiomes Metabolizes *trans*-4-Hydroxy-L-proline. *Science* **2017**, *355*, eaai8386.
(10) Hawkins, C. L.; Davies, M. J. Generation and Propagation of Radical Reactions on Proteins. *Biochim. Biophys. Acta, Bioenerg.* **2001**, *1504*, 196−219.
(11) Yu, D.; Rauk, A.; Armstrong, D. A. Radicals and Ions of Glycine: An Ab initio Study of the Structures and Gas-Phase Thermochemistry. *J. Am. Chem. Soc.* **1995**, *117*, 1789−1796.
(12) Rauk, A.; Yu, D.; Armstrong, D. A. Toward Site Specificity of Oxidative Damage in Proteins: C-H and C-C Bond Dissociation Energies and Reduction Potentials of the Radicals of Alanine, Serine, and Threonine Residues-An Ab initio Study. *J. Am. Chem. Soc.* **1997**, *119*, 208−217.
(13) Block, D. A.; Yu, D.; Armstrong, D. A.; Rauk, A. On the Influence of Secondary Structure on the α-C-H Bond Dissociation Energy of Proline Residues in Proteins: A Theoretical Study. *Can. J. Chem.* **1998**, *76*, 1042−1048.
(14) Rauk, A.; Yu, D.; Taylor, J.; Shustov, G. V.; Block, D. A.; Armstrong, D. A. Effects of Structure on RC-H Bond Enthalpies of Amino Acid Residues: Relevance to H Transfers in Enzyme Mechanisms and in Protein Oxidation. *Biochemistry* **1999**, *38*, 9089−9096.
(15) Green, M. C.; Dubnicka, L. J.; Davis, A. C.; Rypkema, H. A.; Francisco, J. S.; Slipchenko, L. V. Thermodynamics and Kinetics for the Free Radical Oxygen Protein Oxidation Pathway in a Model for β-Structured Peptides. *J. Phys. Chem. A* **2016**, *120*, 2493−2503.
(16) Chu, I. K.; Rodriquez, C. F.; Lau, T. C.; Hopkinson, A. C.; Siu, K. W. M. Molecular Radical Cations of Oligopeptides. *J. Phys. Chem. B* **2000**, *104*, 3393−3397.
(17) Gatlin, C. L.; Tureček, F.; Vaisar, T. Copper(II) Amino Acid Complexes in the Gas Phase. *J. Am. Chem. Soc.* **1995**, *117*, 3637−3638.
(18) Tureček, F. Copper-Biomolecule Complexes in the Gas Phase. The Ternary Way. *Mass Spectrom. Rev.* **2007**, *26*, 563−582.
(19) Tureček, F.; Julian, R. R. Peptide Radicals and Cation-Radicals in the Gas Phase. *Chem. Rev.* **2013**, *113*, 6691−6733.
(20) Martens, J.; Grzetic, J.; Berden, G.; Oomens, J. Structural Identification of Electron Transfer Dissociation Products in Mass Spectrometry Using Infrared Ion Spectroscopy. *Nat. Commun.* **2016**, *7*, 11754.
(21) Nguyen, H. T. H.; Shaffer, C. J.; Pepin, R.; Tureček, F. UV Action Spectroscopy of Gas-Phase Peptide Radicals. *J. Phys. Chem. Lett.* **2015**, *6*, 4722−4727.
(22) Viglino, E.; Shaffer, C. J.; Tureček, F. UV-VIS Action Spectroscopy and Structures of Tyrosine Peptide Cation Radicals in the Gas Phase. *Angew. Chem., Int. Ed.* **2016**, *55*, 7469−7473.
(23) Zubarev, R. A. Reactions of Polypeptide Ions with Electrons in the Gas Phase. *Mass Spectrom. Rev.* **2003**, *22*, 57−77.
(24) Zubarev, R. A.; Kelleher, N. L.; McLafferty, F. W. Electron Capture Dissociation of Multiply Charged Protein Cations. A Nonergodic Process. *J. Am. Chem. Soc.* **1998**, *120*, 3265−3266.
(25) Syka, J. E. P.; Coon, J. J.; Schroeder, M. J.; Shabanowitz, J.; Hunt, D. F. Peptide and Protein Sequence Analysis by Electron Transfer Dissociation Mass Spectrometry. *Proc. Natl. Acad. Sci. U. S. A.* **2004**, *101*, 9528−9533.
(26) Chu, I. K.; Siu, C.-K.; Lau, J. K.-C.; Tang, W. K.; Mu, X.; Lai, C. K.; Guo, X.; Wang, X.; Li, N.; Yao, Z.; et al. Proposed Nomenclature for Peptide Ion Fragmentation. *Int. J. Mass Spectrom.* **2015**, *390*, 24−27.
(27) Yates, B. F.; Bouma, W. J.; Radom, L. Distonic Radical Cations. Guidelines for the Assessment of Their Stability. *Tetrahedron* **1986**, *42*, 6225−6234.
(28) Hammerum, S. Distonic Radical Cations in Gaseous and Condensed Phase. *Mass Spectrom. Rev.* **1988**, *7*, 123−202.
(29) Swaney, D. L.; McAlister, G. C.; Wirtala, M.; Schwartz, J. C.; Syka, J. E. P.; Coon, J. J. Supplemental Activation Method for Highly Efficient Electron Transfer Dissociation of Doubly Protonated Peptide Precursors. *Anal. Chem.* **2007**, *79*, 477−485.
(30) Xia, Y.; Han, H.; McLuckey, S. A. Activation of Intact Electron-Transfer Products of Polypeptides and Proteins in Cation Transmission Mode Ion/Ion Reactions. *Anal. Chem.* **2008**, *80*, 1111−1117.
(31) Brodbelt, J. S. Photodissociation Mass Spectrometry: New Tools for Characterization of Biological Molecules. *Chem. Soc. Rev.* **2014**, *43*, 2757−2783.
(32) Ledvina, A. R.; McAlister, G. C.; Gardner, M. W.; Smith, S. I.; Madsen, J. A.; Schwartz, J. C.; Stafford, G. C., Jr.; Syka, J. E. P.; Brodbelt, J. S.; Coon, J. J. Infrared Photoactivation Reduces Peptide Folding and Hydrogen-Atom Migration Following ETD Tandem Mass Spectrometry. *Angew. Chem., Int. Ed.* **2009**, *48*, 8526−8528.
(33) Ledvina, A. R.; Beauchene, N. A.; McAlister, G. C.; Syka, J. E. P.; Schwartz, J. C.; Griep-Raming, J.; Westphall, M. S.; Coon, J. J. Activated Ion Electron Transfer Dissociation Improves the Ability of Electron Transfer Dissociation to Identify Peptides in a Complex Mixture. *Anal. Chem.* **2010**, *82*, 10068−10074.
(34) Pepin, R.; Layton, E. D.; Liu, Y.; Afonso, C.; Tureček, F. Where Does the Electron Go? Stable and Metastable Peptide Cation Radicals Formed by Electron Transfer. *J. Am. Soc. Mass Spectrom.* **2017**, *28*, 164−181.
(35) Antoine, R.; Dugourd, P. Visible and Ultraviolet Spectroscopy of Gas Phase Protein Ions. *Phys. Chem. Chem. Phys.* **2011**, *13*, 16494−16509.
(36) Antoine, R.; Dugourd, P. UV-Visible Activation of Biomolecular Ions. (Laser Photodissociation and Spectroscopy of Mass-Separated Biomolecular Ions). *Lect. Notes Chem.* **2013**, *83*, 93−116.
(37) Chung, T. W.; Hui, R.; Ledvina, A. R.; Coon, J. J.; Tureček, F. Cascade Dissociations of Peptide Cation-Radicals. Part 1. Scope and Effects of Amino Acid Residues in Penta-, Nona- and Decapeptides. *J. Am. Soc. Mass Spectrom.* **2012**, *23*, 1336−1350.
(38) Nguyen, H. T. H.; Tureček, F. Near-UV Photodissociation of Tryptic Peptide Cation Radicals. Scope and Effects of Amino Acid Residues and Radical Sites. *J. Am. Soc. Mass Spectrom.* **2017**, *29*, DOI: 10.1007/s13361-016-1586-7.
(39) Chung, T. W.; Tureček, F. Backbone and Side-Chain Specific Dissociations of *z* Ions from Non-Tryptic Peptides. *J. Am. Soc. Mass Spectrom.* **2010**, *21*, 1279−1295.
(40) Ledvina, A. R.; Chung, T. W.; Hui, R.; Coon, J. J.; Tureček, F. Cascade Dissociations of Peptide Cation-Radicals. Part 2. Infrared Multiphoton Dissociation and Mechanistic Studies of z-Ions from Pentapeptides. *J. Am. Soc. Mass Spectrom.* **2012**, *23*, 1351−1363.
(41) Thomas, D. A.; Sohn, C. H.; Gao, J.; Beauchamp, J. L. Hydrogen Bonding Constrains Free Radical Reaction Dynamics at Serine and Threonine Residues in Peptides. *J. Phys. Chem. A* **2014**, *118*, 8380−8392.
(42) Nguyen, H. T. H.; Shaffer, C. J.; Ledvina, A.; Coon, J. J.; Tureček, F. Serine Effects on Collision-Induced Dissociation and Photodissociation of Peptide Cation Radicals of the $z^{+\bullet}$ Type. *Int. J. Mass Spectrom.* **2015**, *378*, 20−30.
(43) Moss, C. L.; Chamot-Rooke, J.; Brown, J.; Campuzano, I.; Richardson, K.; Williams, J.; Bush, M.; Bythell, B.; Paizs, B.; Tureček, F.; Nicol, E. Assigning Structures to Gas-Phase Peptide Cations and Cation-Radicals. An Infrared Multiphoton Dissociation, Ion Mobility, Electron Transfer and Computational Study of a Histidine Peptide Ion. *J. Phys. Chem. B* **2012**, *116*, 3445−3456.
(44) Pepin, R.; Laszlo, K. J.; Marek, A.; Peng, B.; Bush, M. F.; Lavanant, H.; Afonso, C.; Turecek, F. Toward a Rational Design of Highly Folded Peptide Cation Conformations. 3D Gas-Phase Ion Structures and Ion Mobility Characterization. *J. Am. Soc. Mass Spectrom.* **2016**, *27*, 1647−1660.
(45) Frisch, M. J.; Trucks, G. W.; Schlegel, H. B.; Scuseria, G. E.; Robb, M. A.; Cheeseman, J. R.; Scalmani, G.; Barone, V.; Mennucci,

DOI: 10.1021/acs.jpcb.7b04661
J. Phys. Chem. B 2017, 121, 6557−6569

B.; Petersson, G. A., et al. *Gaussian 09*, Revision A.02; Gaussian Inc.: Wallingford CT, 2009.
(46) Becke, A. D. New Mixing of Hartree-Fock and Local Density-Functional Theories. *J. Chem. Phys.* **1993**, *98*, 1372−1377.
(47) Becke, A. D. Density Functional Thermochemistry. III. The Role of Exact Exchange. *J. Chem. Phys.* **1993**, *98*, 5648−5652.
(48) Møller, C.; Plesset, M. S. A Note on an Approximation Treatment for Many-Electron Systems. *Phys. Rev.* **1934**, *46*, 618−622.
(49) Schlegel, H. B. Potential Energy Curves Using Unrestricted M? ller-Plesset Perturbation Theory with Spin Annihilation. *J. Chem. Phys.* **1986**, *84*, 4530.
(50) Mayer, I. Spin-projected UHF method. IV. Comparison of Potential Curves Given by Different One-Electron Methods. *Adv. Quantum Chem.* **1980**, *12*, 189−262.
(51) Chai, J. D.; Head-Gordon, M. Systematic Optimization of Long-Range Corrected Hybrid Density Functionals. *J. Chem. Phys.* **2008**, *128*, 084106.
(52) Chai, J. D.; Head-Gordon, M. Long-Range Corrected Hybrid Density Functionals with Damped Atom-Atom Dispersion Corrections. *Phys. Chem. Chem. Phys.* **2008**, *10*, 6615−6620.
(53) Zhao, Y.; Truhlar, D. G. The M06 Suite of Density Functionals for Main Group Thermochemistry, Thermochemical Kinetics, Noncovalent Interactions, Excited States, and Transition Elements: Two New Functionals and Systematic Testing of Four M06-Class Functionals and 12 Other Functionals. *Theor. Chem. Acc.* **2008**, *120*, 215−241.
(54) Stewart, J. J. P. Optimization of Parameters for Semi-Empirical Methods. V. Modification of NDDO Approximations and Application to 70 Elements. *J. Mol. Model.* **2007**, *13*, 1173−1213.
(55) Řezáč, J.; Fanfrlík, J.; Salahub, D.; Hobza, P. Semi-Empirical Quantum Chemical PM6Method Augmented by Dispersion and H-Bonding Correction Terms Reliably Describes Various Types of Noncovalent Complexes. *J. Chem. Theory Comput.* **2009**, *5*, 1749−1760.
(56) Stewart, J. J. P. *MOPAC 16*; Stewart Computational Chemistry: Colorado Springs, CO, USA.
(57) Rezac, J. Cuby: An Integrative Framework for Computational Chemistry. *J. Comput. Chem.* **2016**, *37*, 1230−1237.
(58) Furche, F.; Ahlrichs, A. Adiabatic Time-Dependent Density Functional Methods for Excited State Properties. *J. Chem. Phys.* **2002**, *117*, 7433−7447.
(59) Iikura, H.; Tsuneda, T.; Yanai, T.; Hirao, K. A Long-Range Correction Scheme for Generalized-Gradient-Approximation Exchange Functionals. *J. Chem. Phys.* **2001**, *115*, 3540−3544.
(60) Turecek, F. Benchmarking Electronic Excitation Energies and Transitions in Peptide Radicals. *J. Phys. Chem. A* **2015**, *119*, 10101−10111.
(61) Sekino, H.; Bartlett, R. J. A Linear Response, Coupled-Cluster Theory for Excitation Energy. *Int. J. Quantum Chem.* **1984**, *26*, 255−265.
(62) Comeau, D. C.; Bartlett, R. J. The Equation-of-Motion Coupled-Cluster Method. Applications to Open- and Closed-Shell Reference States. *Chem. Phys. Lett.* **1993**, *207*, 414−423.
(63) Barbatti, M.; Aquino, A. J.; Lischka, H. The UV Absorption of Nucleobases: Semi-classical Ab initio Spectra Simulations. *Phys. Chem. Chem. Phys.* **2010**, *12*, 4959−4967.
(64) Barbatti, M.; Ruckenbauer, M.; Plasser, F.; Pittner, J.; Granucci, G.; Persico, M.; Lischka, H. Newton-X: A Surface-Hopping Program for Nonadiabatic Molecular Dynamics. *Wiley Interdisciplinary Reviews: Comput. Mol. Sci.* **2014**, *4*, 26−33.
(65) Gilbert, R. G.; Smith, S. C. *Theory of Unimolecular and Recombination Reactions*; Blackwell Scientific Publications: Oxford, 1990; pp 52−132.
(66) Zhu, L.; Hase, W. L.: *Quantum Chemistry Program Exchange*; Indiana University: Bloomington, 1994; Program No. QCPE 644.
(67) Frank, A. J.; Sadílek, M.; Ferrier, J. G.; Tureček, F. Sulfur Oxoacids and Radicals in the Gas Phase. A Variable-Time Neutralization-Photoexcitation- Reionization Mass Spectrometric and Ab initio/RRKM Study. *J. Am. Chem. Soc.* **1997**, *119*, 12343−12353.
(68) Osburn, S.; Berden, G.; Oomens, J.; O'Hair, R. A. J.; Ryzhov, V. Structure and Reactivity of the N-Acetyl-Cysteine Radical Cation and Anion: Does Radical Migration Occur? *J. Am. Soc. Mass Spectrom.* **2011**, *22*, 1794−1803.
(69) Hao, Q.; Song, T.; Ng, D. C. M.; Quan, Q.; Siu, C. K.; Chu, I. K. Arginine Facilitated Isomerization: Radical-Induced Dissociation of Aliphatic Radical Cationic Glycylarginyl(iso)leucine Tripeptides. *J. Phys. Chem. B* **2012**, *116*, 7627−7634.
(70) Zhao, J.; Song, T.; Xu, M.; Quan, Q.; Siu, K. W. M.; Hopkinson, A. C.; Chu, I. K. Intramolecular Hydrogen Atom Migration along the Backbone of Cationic and Neutral Radical Tripeptides and Subsequent Radical-Induced Dissociations. *Phys. Chem. Chem. Phys.* **2012**, *14*, 8723−8731.
(71) Osburn, S.; Berden, G.; Oomens, J.; O'Hair, R. A. J.; Ryzhov, V. S-to-αC Radical Migration in the Radical Cations of Gly-Cys and Cys-Gly. *J. Am. Soc. Mass Spectrom.* **2012**, *23*, 1019−1023.
(72) Laskin, J.; Kong, R. P. W.; Song, T.; Chu, I. K. Effect of the Basic Residue on the Energetics and Dynamics of Dissociation of Phosphopeptides. *Int. J. Mass Spectrom.* **2012**, *330*−*332*, 295−301.
(73) Zhang, X.; Julian, R. R. Exploring Radical Migration Pathways in Peptides with Positional Isomers, Deuterium Labeling, and Molecular Dynamics Simulations. *J. Am. Soc. Mass Spectrom.* **2013**, *24*, 524−533.
(74) Osburn, S.; Berden, G.; Oomens, J.; Gulyuz, K.; Polfer, N. C.; O'Hair, R. A. J.; Ryzhov, V. Structure and Reactivity of the Glutathione Radical Cation: Radical Rearrangement from the Cysteine Sulfur to the Glutamic Acid α-Carbon Atom. *ChemPlusChem* **2013**, *78*, 970−978.
(75) Lai, C.-K.; Mu, X.; Hao, Q.; Hopkinson, A. C.; Chu, I. K. Formation, Isomerization, and Dissociation of ε- and α-Carbon-Centered Tyrosyl Glycyl Glycine Radical Cations. *Phys. Chem. Chem. Phys.* **2014**, *16*, 24235−24243.
(76) Xu, M.; Tang, W.-K.; Mu, X.; Ling, Y.; Siu, C.-K.; Chu, I. K. α-Radical Induced CO2 Loss from the Aspartic Acid Side Chain of the Collisionally Induced Tripeptide Aspartylglycylarginine Radical Cation. *Int. J. Mass Spectrom.* **2015**, *390*, 56−62.
(77) Lesslie, M.; Osburn, S.; van Stipdonk, M. J.; Ryzhov, V. Gas-Phase Tyrosine-to-Cysteine Radical Migration in Model Systems. *Eur. Mass Spectrom.* **2015**, *21*, 589−597.
(78) Osburn, S.; Chan, B.; Ryzhov, V.; Radom, L.; O'Hair, R. A. J. Role of Hydrogen Bonding on the Reactivity of Thiyl Radicals: A Mass Spectrometric and Computational Study Using the Distonic Radical Ion Approach. *J. Phys. Chem. A* **2016**, *120*, 8184−8189.
(79) Pepin, R.; Tureček, F. Kinetic Ion Thermometers for Electron Transfer Dissociation. *J. Phys. Chem. B* **2015**, *119*, 2818−2826.
(80) Gonzalez, C.; Schlegel, H. B. An Improved Algorithm for Reaction Path Following. *J. Chem. Phys.* **1989**, *90*, 2154−2161.
(81) Lifshitz, C. Time-Resolved Appearance Energies, Breakdown Graphs, and Mass Spectra: The Elusive Kinetic Shift. *Mass Spectrom. Rev.* **1982**, *1*, 309−340.
(82) Laskin, J.; Futrell, J. H.; Chu, I. K. Is Dissociation of Peptide Cation-Radicals an Ergodic Process? *J. Am. Chem. Soc.* **2007**, *129*, 9598−9599.

DOI: 10.1021/acs.jpcb.7b04661
J. Phys. Chem. B 2017, 121, 6557−6569